Supplementary Information for

Combinatorial Screening of Triple Ionic-Electronic Conducting Oxide Perovskite Electrodes for Fuel Cell and Electrolysis Applications

Meagan Papac,[1,2] Jake Huang,[1] Andriy Zakutayev,[2,1] and Ryan O'Hayre[1]

[1]Metallurgical and Materials Engineering Department, Colorado School of Mines, Golden, CO
[2]Materials Science Center, National Renewable Energy Laboratory, Golden, CO

Target synthesis

Oxide targets of the following compositions were synthesized for pulsed laser deposition: $BaZr_{0.6}Y_{0.3}Fe_{0.1}O_{3-\delta}$, $BaZr_{0.1}Fe_{0.9}O_{3-\delta}$, $BaZr_{0.1}Co_{0.9}O_{3-\delta}$, $BaZr_{0.9}Co_{0.1}O_{3-\delta}$, $BaZr_{0.8}Y_{0.2}O_{3-\delta}$, and $BaZr_{0.1}Y_{0.1}Co_{0.3}Fe_{0.5}O_{3-\delta}$. First, ceramic powders were synthesized using a sol-gel method, described in more detail elsewhere.[1] The powder was ground with 10% PVA binder and pressed into 32 mm diameter pellets. These pellets were sintered at 1050-1150°C for 10-15 hours, depending on composition, to achieve crystalline targets (Figure S1).

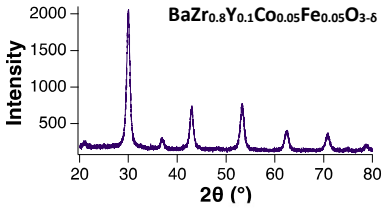

Figure S1. Representative XRD pattern of one of the pulsed laser deposition target compositions.

Thin film XRD

XRD of all thin films from this study showed that this material displays a cubic perovskite structure across the entire chemical composition space of interest (Figure S2).

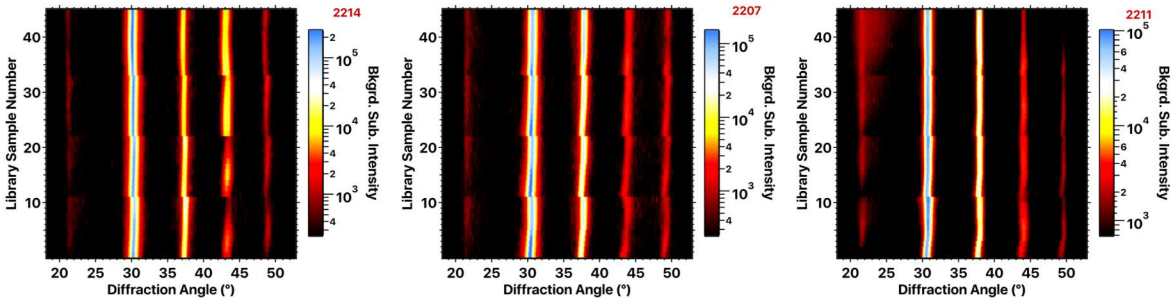

Figure S2. XRD patterns of all libraries presented in this study. Each displays the peaks associated with a cubic perovskite structure and no additional peaks. The colorscale represents intensity with the substrate background subtracted.

Ba concentration

A-site barium concentration can have a non-negligible effect on materials properties.[2] However, in these libraries no correlation was found between Ba concentration and materials properties, location on substrate (Figure S3a), or B-site composition (Figure S3b).

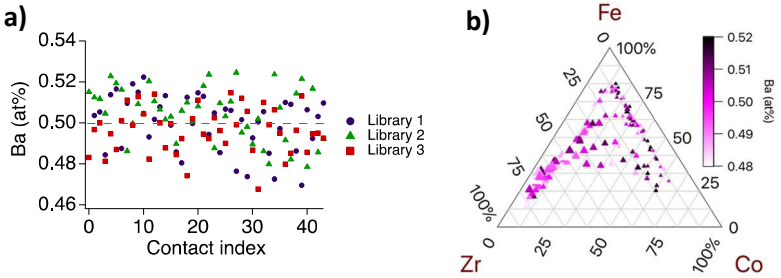

Figure S3. Barium concentration of the 3 combinatorial libraries in this study across a) all contacts measured by XRF and b) all compositions. No correlation was observed between Ba concentration and position on sample, B-site composition, or materials properties.

Electrolyte impedance and changes in impedance upon inclusion of the BCFZY layer

The highest frequency resistance is similar across all libraries and does not display a trend with chemical composition (Figure S4a). Therefore, it is attributed to the electrolyte/substrate impedance and we have not included this impedance in our main analysis. In all samples, the extracted electrolyte resistance is lower under humid N_2 than under dry air. We also measured the impedance of a film stack with the configuration ITO|BZY|Ti+Au (without the BCFZY electrode layer) and found that the modulus of the impedance is lower under humid N_2 than under dry air (Figure S4b). This is the expected behaviour of a proton-conducting layer.

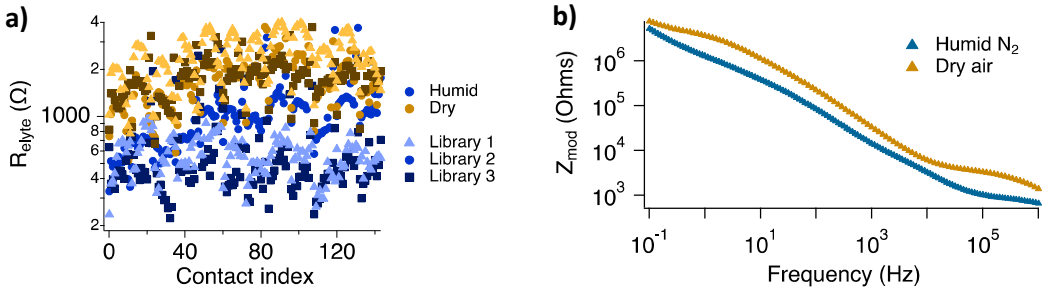

Figure S4. a) Electrolyte resistance, as determined by the ECM fit. The resistance is higher under dry air compared to humid N_2, due to increased bulk proton conductivity of BZY20 under humid conditions. b) Similarly, the modulus of the impedance measured directly on a BZY20 electrolyte film is lower under the humid versus dry condition across all frequencies.

Nyquist plots of the data from this sample clearly show blocking electrode behaviour: we see a consistent rise in impedance with decreasing frequency that indicates an imperfectly blocking interface (Figure S5a). The low-frequency resistance suggests that the resistance of the electronic pathway is on the order of 1e6 Ohms. In contrast, the films with the ITO|BZY|BCFZY|Ti+Au configuration (Figure S5b) show very different behaviour: the total resistance is 3 to 4 orders of magnitude smaller and the imaginary impedance approaches zero at low frequencies, indicating that the blocking interface is no longer present. This suggests that the blocking interface is the BZY|Ti+Au interface and not the ITO|BZY interface.

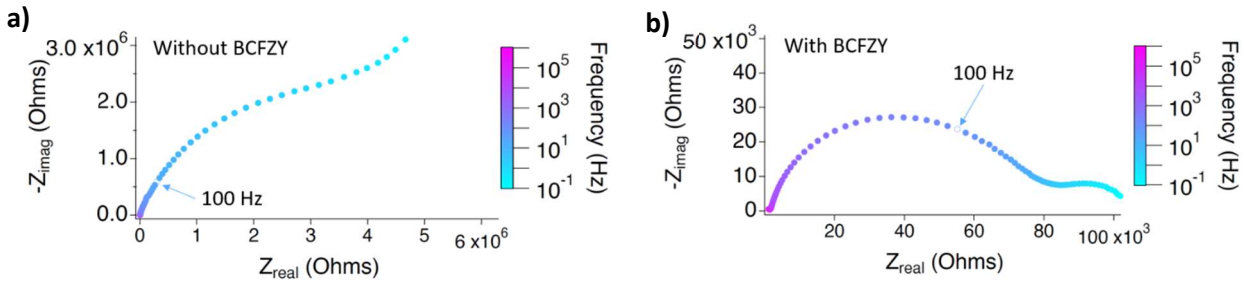

Figure S5. Representative Nyquist plots of a) a BZY film deposited on ITO with metal contacts on top and b) the same film stack with a layer of $BaCo_{.19}Fe_{.15}Zr_{.46}Y_{.20}O_{3-\delta}$ inserted between the BZY and metal contacts. The impedance in the medium-to-low frequency range is much lower in the sample that includes the BCFZY layer.

The BZY|BCFZY film stack shows 2 or 3 additional, low-frequency impedance features that can be resolved, particularly at the highest heater setpoint. In this stack, the imaginary impedance tends toward the real axis at low frequency. Rather than a blocking BZY|metal interface, we have a BZY|BCFZY interface that exchanges ions and a BCFZY|metal interface that exchanges electronic carriers. We also replace the BZY surface with a BCFZY surface that passes ions both directions because water and/or oxygen can be formed or dissociated here. These results suggest both that the ionic pathway dominates

(as evidenced by the dramatic reduction in total resistance) and that the BZY|ITO interface is not completely blocking to ions. Although the reason for this behaviour is unclear, we hypothesize that the large BZY-ITO interfacial area and/or the possibility of some ionic conductivity in the ITO account for the lack of blocking behaviour. We cannot assign each of these processes to a single impedance spectral feature, but it is clear that the processes happening in these samples are not the same as those in the blocking (BZY) case. Thus, we posit that by inserting the BCFZY layer between the BZY and the metal, we remove the impedance contribution of the blocking interface and replace it with BCFZY-related processes that are responsible for R1, R2, and R3. The chemical composition of the BCFZY layer affects transfer at the BZY|BCFZY interface, at the BCFZY|metal interface, at the BCFZY surface, and, perhaps, lateral electronic transfer between the BCFZY|metal interface and the BCFZY surface. Each of these charge-transfer processes is relevant to fuel cell operation. By lowering the polarization resistance of each of these processes, the total polarization resistance is lowered, and we can reasonably expect that fuel cell performance would benefit.

Multidimensional, hierarchical Bayesian equivalent circuit model

To enable consistent, robust optimization of the activated equivalent circuit model defined in Section 4, hierarchical Bayesian prior distributions are employed. Briefly, Bayesian models use prior distributions (typically referred to simply as "priors") to express prior beliefs about the model parameters – i.e., characteristics that we expect the parameters to exhibit *before* observing the data. For example, we may expect that a certain parameter is usually small, or that errors are normally distributed. These priors are balanced with the data via Bayes' Theorem to obtain the posterior distribution, which reflects the most likely solution given both the prior beliefs and the data. In most cases, an analytic expression for the posterior distribution cannot be obtained. Instead, the posterior distribution may be estimated via Monte Carlo sampling. Alternatively, the mode of the posterior distribution may be estimated via non-linear optimization, which incurs a substantially lower computational cost than Monte Carlo sampling. A common and simple example of Bayesian priors in action is ridge regression, which is much more robust than ordinary linear regression for high-dimensional optimizations.

Here we define the priors employed for the hierarchical Bayesian activated equivalent circuit model. Prior to optimization, the impedance data is scaled:

$$\boldsymbol{Z}^* = \boldsymbol{Z} \cdot \frac{\sqrt{N}}{\mathrm{std}(|\boldsymbol{Z}|)}$$

where $\boldsymbol{Z}^*$ is the vector of scaled impedance values, $\boldsymbol{Z}$ is the vector of measured impedance values, N is the number of measured frequencies, and $|\boldsymbol{Z}|$ is the vector of measured impedance modulus values. This ensures a consistent scale for the data and model parameters such that the priors do not need to be adjusted. Model parameters marked with an asterisk superscript are affected by the impedance scaling; these parameters are optimized in their scaled form, and thus must be multiplied by the inverse of the impedance scaling factor after optimization to obtain the true values.

The magnitude of each HN element is controlled via two hierarchical priors:

$$R^*_{\mathrm{base},k} \sim Normal\left(0, s_{R_k}\right) \quad \text{for } k \in [1, K],$$

$$s_{R_k} \sim Inverse\ Gamma\left(\alpha_{R_k}, \beta_{R_k}\right) \quad \text{for } k \in [1, K].$$

This notation indicates that the parameter $R^*_{\text{base},k}$ follows a normal distribution with mean 0 and scale (standard deviation) s_{R_k}, while the scale parameter s_{R_k} itself follows an inverse gamma distribution with shape and rate parameters α_{R_k} and β_{R_k}, respectively. The values of α_{R_k} and β_{R_k} were fixed at 1 and 2, respectively, for all optimizations. Meanwhile, the shift parameter ϕ_k is drawn from a log-normal distribution:

$$\phi_k \sim Log\ Normal\left(0, s_{\phi_k}\right) \quad \text{for } k \in [1, K].$$

The log-normal distribution ensures that ϕ_k is centered at 1 (i.e., 1 is the most likely value). The value of s_{ϕ_k} was fixed at 0.2 for all optimizations.

To describe the equilibration of the sample, an equilibrating ZARC element is included in the model. The impedance of a stable ZARC element is given by

$$Z_{\text{ZARC}}(\omega) = \frac{R}{1 + (j\omega\tau_0)^{\beta}},$$

where R, τ_0, and β have the same meaning as for the HN element. Time dependence is added to the equilibrating ZARC element by defining its resistance as

$$R_{\text{equil}}(t) = R_{\text{equil},f}\left(\frac{t - t_i}{t_f - t_i}\right),$$

where t_i and t_f are the measurement start and end times, respectively, and $R_{\text{equil}}(t)$ changes linearly from zero at the start of the measurement (highest frequency) to $R_{\text{equil},f}$ at the end of the measurement (lowest frequency). Although the true time dependence of the equilibration process is expected to be nonlinear, a linear approximation is reasonable when the timescale of the equilibration is longer than that of the measurement. In addition, the linear approximation reduces the number of parameters required to describe the equilibrating element and simplifies optimization of the model. The values of τ_0 and β are fixed with respect to time. The magnitude of the equilibration contribution at each temperature is strongly penalized via two hierarchical priors:

$$R^*_{\text{drift},f,p} \sim Normal\left(0, s_{R_{\text{drift},p}}\right) \quad \text{for } p \in [1, P],$$

$$s_{R_{\text{drift},p}} \sim Normal\left(0, \sigma_{s_{\text{drift},p}}\right) \quad \text{for } p \in [1, P].$$

Unlike for the HN resistances, the scale parameter $s_{R_{\text{drift},p}}$ is drawn from a normal distribution, rather than an inverse gamma distribution, to further reduce magnitude. The value of $\sigma_{s_{\text{drift},p}}$ was fixed at 0.05 for all dry air spectra and 0.2 for all humid N_2 spectra. $R_{\text{equil},f}$ may be either positive or negative, as the impedance of the sample may increase or decrease over time.

Weak priors are applied to the ohmic resistance and inductance to prevent extreme values:

$$R^*_{\infty,\text{base}} \sim Normal(0,100),$$

$$L^* \sim Normal(0,1).$$

The remaining priors describe the impedance error structure. The error model and priors defined by Equations 30a-30f of ref. [3] are again employed here.

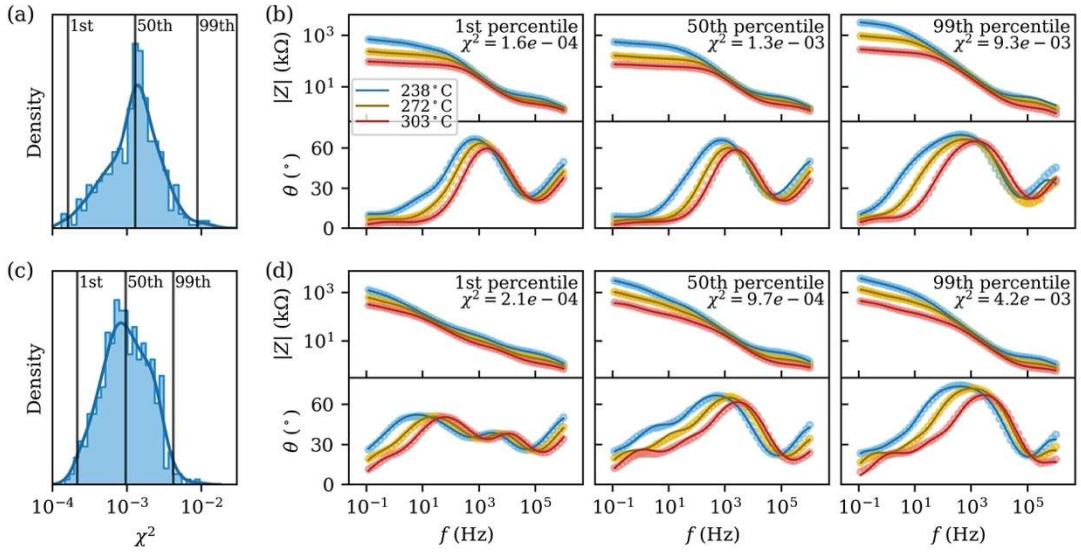

Figure S6. Validation of activated ECM fits. (a, c) Distribution of χ^2 values for ECM fits in dry air (a) and humid N2 (b). χ^2 values were calculated using modulus weighting across all temperatures. The smooth blue line is a kernel density estimate of the distribution. The vertical black lines indicate the 1st, 50th, and 99th percentiles of χ^2, respectively, from left to right. (b, d) Bode plots of the activated ECM fits corresponding to the 1st, 50th, and 99th percentiles of χ^2 in dry air (b) and humid N2 (d). Circles indicate measured data points, while lines indicate fits. For visual clarity, every second data point from each spectrum is shown.

Changes in DRT spectra with increasing hydration

At frequencies below 100 Hz, the impedance changes slowly enough under humidified N_2 that the changes are measurable by a series of impedance measurements. The high-frequency process either is unaffected or, more likely, acclimates quickly enough that any change is not readily observable at the relevant time scales.

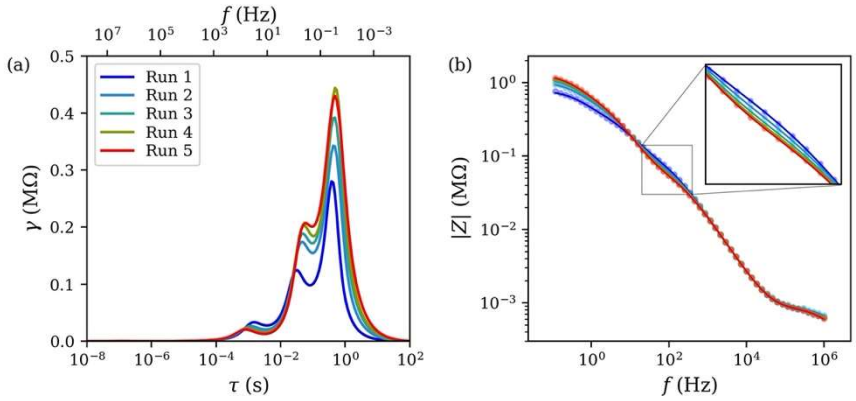

Figure S7. Representative example of repeated measurements under humid N_2. Collection of the first EIS spectrum commenced immediately after humid N_2 began flowing; each subsequent measurement began when the previous measurement finished. (a) DRTs obtained from repeated EIS measurements. R_1 decreases over time, while R_2 and R_3 increase over time. (b) Impedance modulus for repeated EIS measurements. In the frequency range corresponding to R_1, ~10-500 Hz, the modulus decreases over time (inset). At frequencies below 10 Hz, the modulus increases over time. For visual clarity, every second data point is shown.

In the humid, reducing condition, the impedance increases with time at the lowest frequencies (below 10 Hz) and decreases with time at frequencies between 10 and 100 Hz (Figure S7). The oxygen surface reaction impedance increases as water fills the oxygen vacancies and the oxygen reactant becomes limiting in the reducing atmosphere. This may be the cause of the low-frequency impedance increase. The proton-related process has a decreased resistance due to the increased concentration of protons and the charge-transfer resistance is also decreased due to the increased number of charge carriers due to filling oxygen vacancies. These changes with increased hydration may explain the decreased impedance in the mid-frequency range.

Capacitance of each DRT peak

Under dry air, the capacitance values (Figure S8) are low for the high-frequency peak (assigned to the electrolyte), medium-valued and similar for peaks 1 and 2, and high for the low-frequency peak. The capacitances of the BZY peak and of Peak 2 are slightly higher under humid N_2 compared to dry air. The capacitance of Peak 1 changes minimally, and Peak 3 is lower in humid N_2.

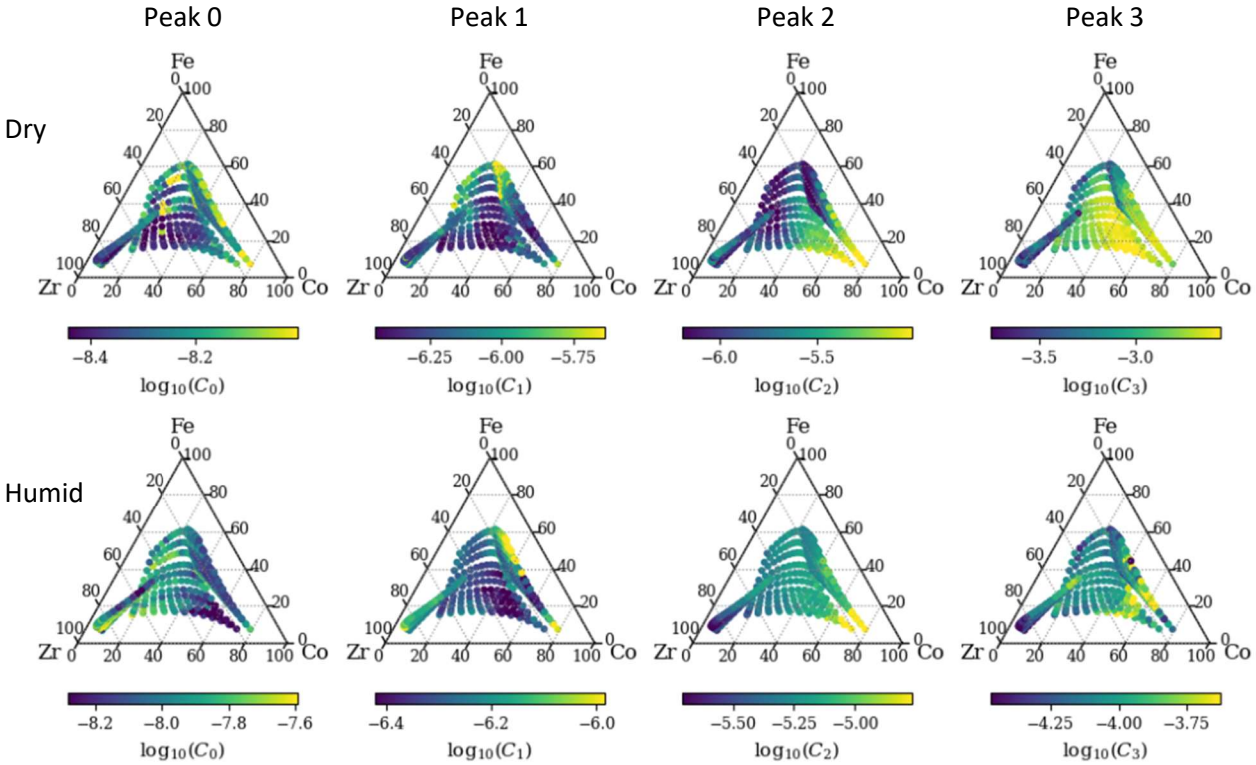

Figure S8. Capacitance of each peak measured under dry air (top) and humidified N2 (bottom) at 303°C. Peak 0, related to the BZY electrolyte layer, has the smallest capacitance. Peaks 1 and 2 have the next smallest capacitances and change only slightly under the humid condition compared to the dry condition. The capacitance of Peak 3 changes most drastically upon the change in gas condition and has the largest capacitance under both conditions.

DC conductivity

DC conductivity was measured from 0 to -1V on BCFZY thin films deposited on ITO and topped with patterned metal contacts (Figure S9a). Under dry air, the conductivity is considerably higher in the Co-rich portion of the ternary. Under humidified N_2, the conductivity is much lower in the compositions with higher Zr/Y concentrations than it is under dry air. This may be due to increased proton uptake and mobility in these compositions. Although the DC conductivity is lower in Zr/Y-rich compositions

compared to Co-rich compositions, this does not induce additional, distinct impedance arcs collected from ITO/BZY/BCFZY/Ti/Au stack samples (Figure S9b).

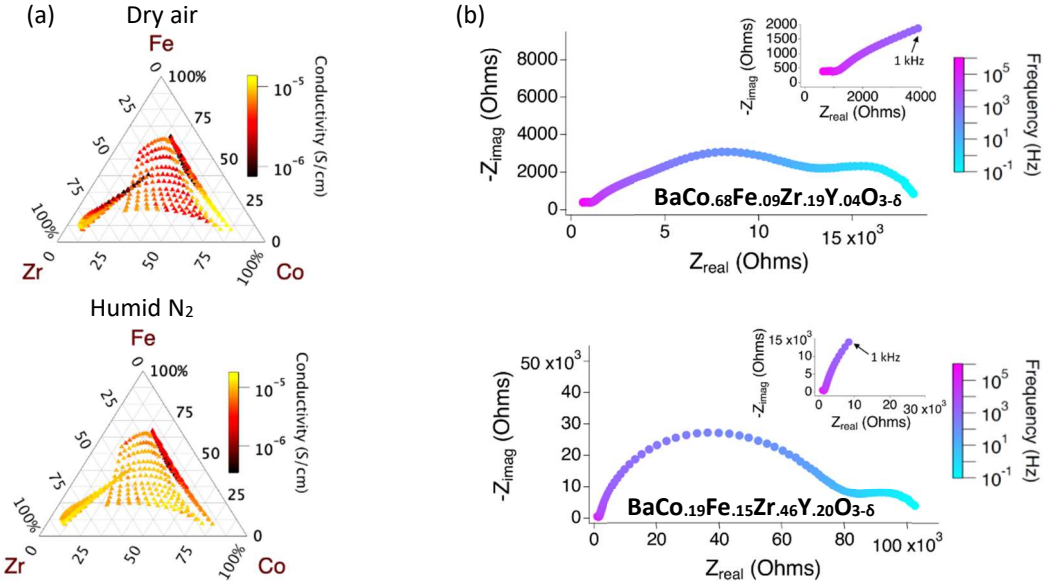

Figure S9. a) Ternary of DC conductivity at 303°C measured on ITO/BCFZY/Ti/Au film stacks with applied voltages from 0 to -1V in dry air and humidified nitrogen. b) Nyquist plots of a Co-rich (top) and a Zr/Y-rich (bottom) composition in ITO/BZY/BCFZY/Ti/Au film stacks measured at 303°C under dry air. Insets: Nyquist plots across the medium-to-high frequency range (minimum 1 kHz).

Nyquist plots with varying cation composition

Raw Nyquist plots provide a very basic way to observe changes in impedance with chemical composition (Figure S10). In both humid and dry gas conditions, impedance decreases with increasing Co:Fe ratio, which may be due to increasing electronic conductivity and higher oxygen vacancy concentration with increasing Co concentration. Under humid conditions, impedance decreases with increasing Zr/Y concentration, while under dry conditions, impedance increases with increasing Zr/Y concentration. This is likely due to increased proton conduction in the humid condition that increases with increasing Y concentration. These results are consistent with our in-depth analysis of total polarization resistance.

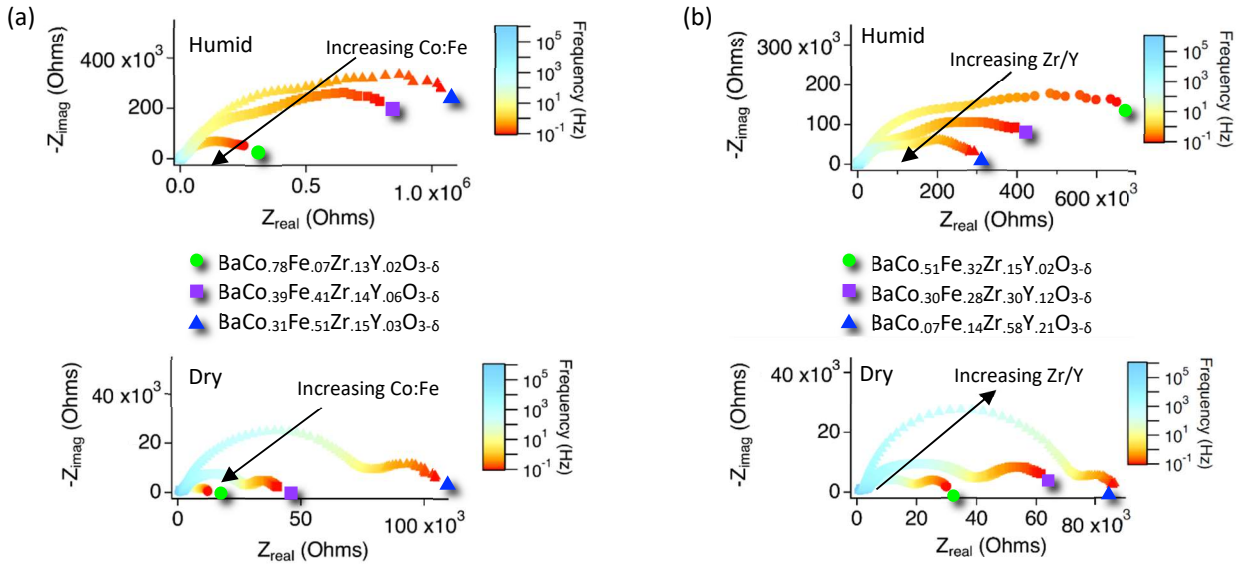

Figure S10. Nyquist plots collected at 303°C under dry air and humidified N2 with a) various Co:Fe ratios and b) Zr/Y concentrations.

Measurements in dry air after exposure to the humidified N_2 gas atmosphere

A set of compositions was measured in dry air after the humidified N_2 measurement. For each sample point, the measurement was repeated 5 times in dry air before the probe was moved to the next sample point. Before each repeated measurement, a 30-second dwell under gas flow equilibrated the sample with the gas environment. The changes in polarization resistance relative to the original dry air measurements are shown below for the re-measured compositions. Because the impedance did not change substantially during each of the 5 repeated measurements, the R_p obtained from the first measurement is represented in the figure below.

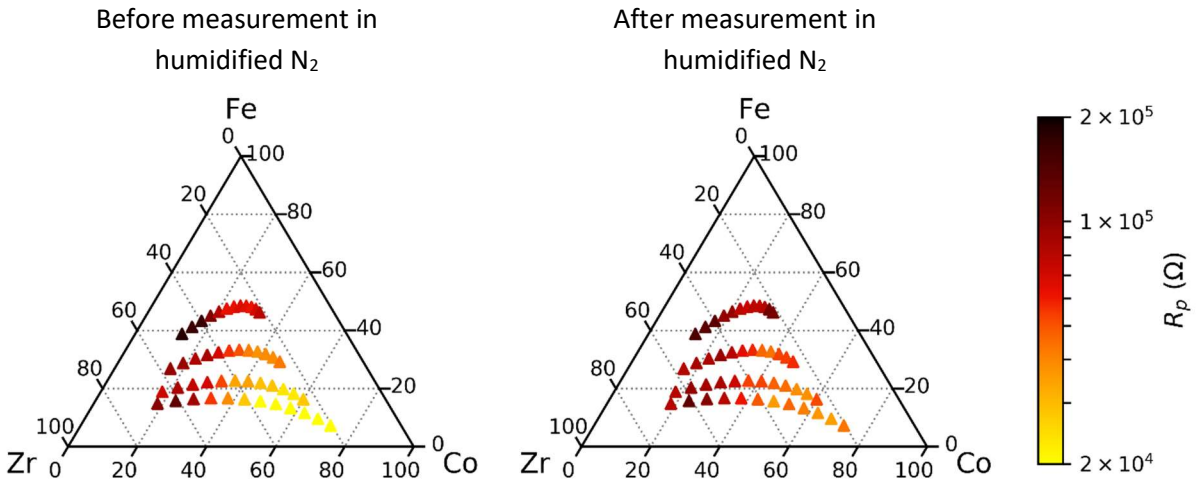

Figure S11. Total polarization resistance (R_p) of a select number of points measured before (left) and after (right) exposure to humidified N_2 and storage in a dry N_2 box for more than 30 days. R_p increases slightly in the Co-rich corner of the ternary, but the overall trend remains the same across the composition space.